Numerical analysis on the local mechanical fields in polycrystalline 316LN stainless steel under cyclic fatigue loading : Comparison with experimental results

Stéphanie Basseville, Georges Cailletaud, T. Ghidossi, Yoann Guilhem, E. Lacoste, Henry Proudhon, L. Signor, P. Villechaise

Stéphanie Basseville, Georges Cailletaud, T. Ghidossi, Yoann Guilhem, E. Lacoste, et al.. Numerical analysis on the local mechanical fields in polycrystalline 316LN stainless steel under cyclic fatigue loading : Comparison with experimental results. Materials Science and Engineering: A, 2017, 696, pp.122-136. 10.1016/j.msea.2017.04.023 . hal-01518940

HAL Id: hal-01518940
https://minesparis-psl.hal.science/hal-01518940

Submitted on 28 Jun 2017

Numerical analysis on the local mechanical fields in polycrystalline 316LN stainless steel under cyclic fatigue loading: comparison with experimental results

S. Basseville[a,b,*], G. Cailletaud[b], T. Ghidossi[c], Y. Guilhem[d], E. Lacoste[c], H. Proudhon[b], L. Signor[c], P. Villechaise[c]

[a] *Université de Versailles-Saint-Quentin-en-Yvelines, 45 avenue des Etats-Unis, 78035 Versailles cedex, France*
[b] *MINES ParisTech, PSL Research University, Centre des Matériaux, CNRS UMR 7633, BP 87, 91003 Evry Cedex, France*
[c] *Institut P', CNRS UPR 3346, ISAE-ENSMA, Université de Poitiers, 11 boulevard Marie et Pierre Curie, BP 30179 86962 Futuroscope Chasseneuil, France*
[d] *Laboratoire de Mécanique et Technologie (LMT), ENS Paris-Saclay/CNRS/Université Paris-Saclay, 61 Avenue du Président Wilson, 94235 Cachan Cedex, France*

Abstract

The present paper is devoted to the study of the parameters responsible for the initiation and/or propagation of transgranular microcracks in polycrystalline materials. The investigation is carried out on an aggregate made of 316LN stainless steel which 3D grain shape and orientation were reconstructed using 2D serial Electron BackScattered Diffraction scans. The evaluation and the analysis of the local mechanical fields at the free surface of the polycrystalline aggregate subjected to cycling loading are performed using Finite Element Crystal Plasticity. Two crystal plasticity models are used and compared through Finite Element computations: quasi-physical or phenomenological models. The local parameters which possibly drive crack initiation are analysed and then compared to the experimental observations. A new criterion predicting whether a specific grain is likely to present a fatigue crack initiation is finally proposed.

Keywords: Polycrystal, 316LN Steel, Crystal plasticity, Finite element, Fatigue

---

1. Introduction

Fatigue life of polycrystalline materials is mainly governed by the early stages of surface short cracks. The stages of initiation and propagation of fatigue microcracks, which may represent from 50 % to 80 % of total component life, have been the subject of various works, (see for instance [1, 2]). Microstructurally Short Cracks (MSCs) having a length of the order of a few grains are governed by the local microstructure. Surface roughness, grain or phase boundaries, inclusions, plastic incompatibilities and persistent slip bands (PSBs) are the main causes of MSC nucleation. Initiation is mainly related to PSBs which growth leads to the appearance of intrusion and extrusion steps at the surface of the specimen also called Persistent Slip Markings (PSMs), see for instance [3–6]. Their direction is governed by crystal plasticity and thus follows slip planes containing slip systems at the surface of the grains. PSMs represent mainly the preferential initiation sites of a transgranular MSC. The microstructure is also the source of a competition between transgranular and intergranular cracks [7]. For polycrystalline 316L or 316LN type stainless steels under low cycle fatigue, transgranular cracks are predominant [8–10]. However, strong misorientations at grain or phase boundaries can decrease the transgranular crack growth and lead to intergranular crack growth [11].

Taking account of all these experimental observations, numerical investigations can help understanding the local behaviour of the material, and promote the development of local physically supported MSC initiation models. Simulation of a real 3D microstructure with hundreds of grains including a real crack loaded for several thousands of cycles is still out of reach. This is why classically authors consider only representative samples on reduced microstructures, like for instance 2D FE simulations on single crystal, bicrystal [12] or polycrystals [13, 14]. When the study is devoted to the free surface effect in polycrystalline aggregate, plastic strain localisation and its spatial organisation on the surface and inside the bulk must be analysed. This is why 3D meshes should be preferentially used (see for instance [15–17]). Numerical results can then be compared to experimental tests [18, 19] or subjected to statistical analysis [16].

The objective of this work is to better understand the local mechanisms that affect MSC initiation. Therefore, the study first focuses on the influence of the constitutive laws on the local mechanical fields. Two categories of models are introduced to describe the behaviour of single crystals: a phenomenological model proposed by Méric and Cailletaud (MC-CP) [20] and a quasi-physical model, named Crystal ECP (ECP-CP) [21, 22]. The importance of the aggregate size for numerical simulations results is briefly

---

[*] Corresponding author.

Email addresses: `stephanie.basseville@uvsq.fr` (S. Basseville), `georges.cailletaud@mines-paristech.fr` (G. Cailletaud), `yoann.guilhem@ens-paris-saclay.fr` (Y. Guilhem)

Preprint submitted to Materials Science and Engineering: A *April 6, 2017*

discussed. The second purpose is to characterise the parameters responsible for the initiation and micro-propagation of transgranular microcracks in 316LN specimen subjected to low cycle fatigue loading using Finite Element Crystal Plasticity (FECP). The simulations correspond to an aggregate located at the free surface during the experimental test described in [10], which was simulated to give a first overview of a limited set of local variables that might be relevant for a crack initiation criterion. Such analysis is now extended by investigating more local variables to provide a more deterministic criterion. Our numerical results will be compared to associated experimental measurements, which will be used as reference. Several parameters of the literature causing crack initiation were analysed, namely the cumulated viscoplastic slip, the von Mises plastic strain, and finally a new criterion that defines when a surface grain is likely to present intrusion-extrusion.

The paper is organised as follows. First, the experimental tests performed in [10] are briefly recalled in section 2 for the sake of completeness. The Finite Element simulations involving two crystal plasticity models previously mentioned are then depicted. The constitutive equations, the material parameters identification, the FE mesh and the boundary conditions are presented in section 3. Finally, several variables able to characterise crack initiation are described in section 4, then analysed and compared to the experimental results in section 5.

2. Experimental description and analyses

This section summarises the main experimental results that are used to reconstruct the polycrystalline aggregate considered in the numerical simulations. More details can be found in [10]. A specimen of a 316LN type austenitic stainless steel was subjected to symmetrical uniaxial tension-compression fatigue test carried out in air, at room temperature, performed with a constant prescribed plastic strain amplitude of $\Delta\varepsilon^p/2 = 2 \times 10^{-3}$ and a constant plastic strain rate of $2 \times 10^{-3}\,\mathrm{s}^{-1}$. Fatigue test was interrupted after 5000 cycles which represent about 20 % of the fatigue life. The flat part on the gauge section of the specimen was observed using Scanning Electron Microscopy (SEM). At this stage, a population of hundreds of cracks (including very small cracks shorter than grain size) was formed, corresponding to a surface crack density of about 110 cracks per mm^2. Figure 1 shows a specific grain, in which transgranular cracks were observed. This local configuration is studied in the following. The crystal orientation of surface grains was measured using Electron Back-Scattered Diffraction (EBSD). The studied grain is labeled “88” in the orientation map (figure 1b).

The polycrystalline microstructure (morphology and crystal orientation of grains) was characterised in 3D using serial sectioning of the specimen combined with EBSD measurements. Material removal is performed by careful mechanical polishing. An EBSD scan was performed between two successive polishing steps, which depth was 3 to 5 µm. Twenty nine successive sections were cut, in order to reach a total depth of about 117 µm. The stack of 2D EBSD maps and the reconstruction of 3D grains was performed following an approach similar to [23–25]. First, individual 2D EBSD maps were cleaned up, resized and roughly aligned using successive indention marks. Then, 2D orientation maps are stacked together to build a 3D image with a size of voxels of 4 µm × 4 µm × 3 µm. 3D grains are defined by the group of contiguous voxels which exhibit a misorientation lower than a given user-specified threshold value (5° in the present case). A single crystal orientation, calculated by averaging orientation of each voxel of one grain (including all the layers), is assigned to this grain.

Table 1: Crystallographic analysis of cracked grain.

Slip System	Order	Schmid factors μ	Angle π
C1	1st	0.499	68.8°
B2	2nd	0.453	71.2°

For the studied grain, slip systems C1 and B2 exhibit the two highest Schmid factors. Their respective values are $\mu_{C1} = 0.499$ and $\mu_{B2} = 0.453$. The theoretical angles π between the trace of each slip plane at surface and the loading axis (i.e. horizontal in figure 1) are computed ($\pi_{C1} = 68.8°$ and $\pi_{B2} = 71.2°$). Theoretical traces of both slip systems are close to the one related to the observed crack in figure 1a. As a consequence, one can hardly identify at this stage which slip system led to crack initiation, even if past studies performed on the same material [26] have demonstrated that the critical slip system has the highest Schmid factor (C1 system in the present case). This point will be discussed in the sequel together with the results of the numerical simulations.

3. Crystal plasticity models

Each grain is considered as a single crystal, with an uniform crystallographic orientation, and the displacement fields are supposed to be continuous at grain boundaries. Therefore, stress discontinuities can appear at these sites, where no specific behaviour or model is added. In the literature, there are two categories of models to describe the behaviour of single crystals:

Phenomenological models , based on internal hardening variables. The material parameters are obtained by comparing the simulations to the macroscopic loading curves. They are able to reproduce the mechanical responses under complex loadings.

Quasi-physical models , where the internal variables are based on dislocation densities. A subset of the material parameters with a physical meaning are deduced from physical measurements. They hardly cover the domain of cyclic or complex loadings.

The first objective is to compare the local mechanical fields resulting of numerical simulations according to the

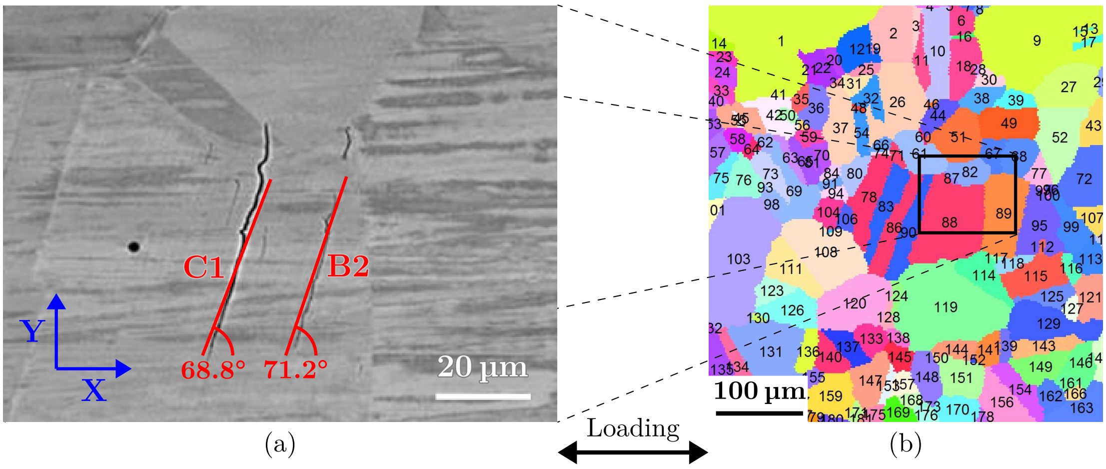

(a) (b)

Figure 1: (a) SEM image of the studied crack and (b) corresponding EBSD map at the free surface (color code in the surface normal direction). Size and location of the SEM image are depicted by a rectangle in the corresponding EBSD map. The loading axis corresponds to the horizontal direction.

constitutive law employed to reproduce the single crystal behaviour. In this paper, the Méric-Cailletaud model (MC-CP) is used as the phenomenological one and the Crystal ECP model (ECP-CP) is used as the quasi-physical one. Both are described in the following sections 3.1 and 3.2.

3.1. Méric–Cailletaud's crystal plasticity model

Méric–Cailletaud's crystal plasticity model ("MC-CP") is introduced in the finite element code Z-set [20]. Small strain assumption is used, which seems reasonable, since, in our past experience, the amount of rotation of a slip plane is around 1° for 1 % macroscopic strain. The total strain rate tensor $\underset{\sim}{\dot{\boldsymbol{\varepsilon}}}$ is composed of an elastic $\underset{\sim}{\dot{\boldsymbol{\varepsilon}}}^e$ and a viscoplastic $\underset{\sim}{\dot{\boldsymbol{\varepsilon}}}^p$ part:

$$\underset{\sim}{\dot{\boldsymbol{\varepsilon}}} = \underset{\sim}{\dot{\boldsymbol{\varepsilon}}}^e + \underset{\sim}{\dot{\boldsymbol{\varepsilon}}}^p = \underset{\approx}{\boldsymbol{C}}^{-1} : \underset{\sim}{\dot{\boldsymbol{\sigma}}} + \underset{\sim}{\dot{\boldsymbol{\varepsilon}}}^p \tag{1}$$

The anisotropic elastic behaviour of grains is included, in order to properly represent the stress state at the onset of plastic flow [27]. The cubic elasticity matrix defined by the fourth order elastic tensor $\underset{\approx}{\boldsymbol{C}}$ is introduced. This elasticity matrix is defined in the crystalline base ([100], [010], [001]) by three coefficients C_{1111}, C_{1122}, and C_{1212} whose values are taken from Huntington [28] (listed in table 2).

$$\underset{\approx}{\boldsymbol{C}} = \begin{pmatrix} C_{1111} & C_{1122} & C_{1122} & 0 & 0 & 0 \\ C_{1122} & C_{1111} & C_{1122} & 0 & 0 & 0 \\ C_{1122} & C_{1122} & C_{1111} & 0 & 0 & 0 \\ 0 & 0 & 0 & C_{1212} & 0 & 0 \\ 0 & 0 & 0 & 0 & C_{1212} & 0 \\ 0 & 0 & 0 & 0 & 0 & C_{1212} \end{pmatrix} \tag{2}$$

The viscoplastic strain rate tensor $\underset{\sim}{\dot{\boldsymbol{\varepsilon}}}^p$ is defined as the sum of the contribution of the 12 octahedral slip systems s for FCC materials:

$$\underset{\sim}{\dot{\boldsymbol{\varepsilon}}}^p = \sum_s \dot{\gamma}^s \underset{\sim}{\boldsymbol{m}}^s \tag{3}$$

Table 2: Elastic materials parameters for 316LN Steel [28].

Law	Cubic elasticity		
Coefficient	C_{1111}	C_{1122}	C_{1212}
Value [MPa]	197 000	125 000	122 000

Each viscoplastic slip rate $\dot{\gamma}^s$ is given according to the crystal plasticity models and depends on the resolved shear stress τ^s, computed on slip system s by means of the orientation tensor $\underset{\sim}{\boldsymbol{m}}^s$:

$$\tau^s = \underset{\sim}{\boldsymbol{\sigma}} : \underset{\sim}{\boldsymbol{m}}^s \tag{4}$$

$$\text{with } \underset{\sim}{\boldsymbol{m}}^s = \frac{1}{2}\left(\underline{\boldsymbol{l}}^s \otimes \underline{\boldsymbol{n}}^s + \underline{\boldsymbol{n}}^s \otimes \underline{\boldsymbol{l}}^s\right) \tag{5}$$

where $\underline{\boldsymbol{n}}^s$ is the normal to the slip plane and $\underline{\boldsymbol{l}}^s$ is the slip direction.

Each viscoplastic slip rate $\dot{\gamma}^s$ is given by a Norton law, function of resolved shear stress τ^s, the critical resolved shear stress τ_0 and two hardening variables; x^s for kinematic and r^s for isotropic hardening.

$$\dot{\gamma}^s = \dot{v}^s \operatorname{sign}\left(\tau^s - x^s\right) \tag{6}$$

$$\dot{v}^s = \left\langle \frac{|\tau^s - x^s| - r^r - \tau_0}{K} \right\rangle^n \tag{7}$$

where K and n are the parameters which define viscosity.

Hardening depends on two internal state variables, namely α^s and ρ^s as described by the nonlinear equations 8 to 11. This framework offers a unique set of active slip systems, and avoids complex procedures attached to the definition of slip activity for the time independent plastic case [29].

$$x^s = c\alpha^s \tag{8}$$

$$r^s = bQ\sum_r h_{sr}\rho^r \tag{9}$$

$$\dot{\alpha}^s = \big(\operatorname{sign}(\tau^s - x^s) - d\alpha^s\big)\dot{v}^s \tag{10}$$

$$\dot{\rho}^s = \big(1 - b\rho^s\big)\dot{v}^s \tag{11}$$

where c and d are material parameters for kinematic hardening, Q and b are material parameters for isotropic hardening. Self-hardening and latent hardening between different slip systems are characterised by the components of the interaction matrix h_{sr}. In the case of octahedral slip systems, six coefficients, each one corresponding to a specific type of interaction, are needed to define this matrix [30]:

h_1: self-hardening of each slip system over itself;

h_2: coplanar interactions between the slip systems defined in the same plane;

h_3: Hirth's junctions acting on slip systems with slip directions orthogonal to each other;

h_4: collinear interactions between each slip system and its deviated slip system, i.e. sharing the same slip direction but a different slip plane;

h_5: glissile junctions relating slip systems sharing the same slip plane as the deviated slip system and as the collinear's deviated slip systems;

h_6: Lomer–Cottrell's locks operating on slip systems which deviated slip system share the same slip plane.

The MC-CP materials parameters were identified using an original set of parameters (with minor modifications) for 316L Steel [17], which is very close to 316LN, and are presented in table 3. The interaction matrix coefficients are deduced after a review of recent studies in the literature on the subject [31–34].

3.2. Crystal ECP model

The Crystal ECP model ("ECP-CP") is implemented in the Finite Element Code ABAQUS [36]. In this case, the crystal plasticity constitutive law uses a large deformation framework, based on the multiplicative decomposition of the deformation gradient into elastic and plastic parts [21, 22].

Each viscoplastic slip rate $\dot{\gamma}^s$ is given by a Pierce-type relationship [21], function of the resolved shear stress τ^s, critical resolved shear stress τ_c^s and reference strain rate $\dot{\gamma}_0^s$:

$$\dot{\gamma}^s = \dot{\gamma}_0^s \left\langle \frac{\tau^s}{\tau_c^s} \right\rangle^n \operatorname{sign}(\tau^s) \tag{12}$$

where n is the viscosity exponent.

The critical resolved shear stress τ_c^s is computed on slip system s and depends on the dislocations density ρ in an Orowan-type relationship:

$$\tau_c^s = \tau_0 + \mu b\sqrt{\sum_r a_{sr}\rho^r} \tag{13}$$

where τ_0 is the initial critical resolved shear stress, μ the shear coefficient, b is the norm of the Burgers vector and a_{sr} the interaction matrix which is defined by the four following coefficients, each linked to the interaction types presented previously:

a_0: self-hardening;

a_1: collinear, coplanar and orthogonal slip systems interactions;

a_2: glissile's junctions;

a_3: Lomer-Cottrell's locks.

The evolution of the dislocation density ρ^s is defined by:

$$\dot{\rho}^s = \frac{|\dot{\gamma}^s|}{b}\left(\frac{\sum_{r\neq s}\rho^r}{K} - g_c\rho^s\right) \tag{14}$$

where K is a material parameter, g_c is proportional to the distance annihilation of dislocations. The identified materials parameters for 316LN Steel are presented in table 4 and provided by Schwartz [37].

3.3. Meshes and boundary conditions

The 3D reconstructed polycrystalline microstructure described in section 2 is used as input of the aggregate mesh building procedure. Each voxel of size 4 µm × 4 µm × 3 µm defines one linear hexahedral finite element with exact integration. From our past experience, this is justified by the fact that using an homogeneous mesh density avoids unwanted local variables localization and scattering in the refined zones [17]. Two meshes corresponding to domains of different sizes, but both including the cracked grain studied in section 2, have been built. The larger one is based on serial 2D EBSD maps whose dimensions are equal to the map reported in figure 1b. In figure 2a (respectively figure 2b), the larger (resp. small) mesh is composed of 386 grains (resp. 157) and has a size of 464 µm × 488 µm × 117 µm (resp. 320 µm × 284 µm × 117 µm). The mesh includes 551 928 elements, 575 640 nodes, or 1 726 920 DOF (resp. 221 520 elements, 233 280 nodes or 699 840 DOF). The studied grain where the crack has initiated is depicted in figure 2c. Its complex morphology is due to two elongated parallel twins which do not fully cross the grain. Thus, this individual grain appears as three distinct grains in the 2D map at surface (red grains 78, 86 and 88 in figure 1).

Boundary conditions are defined to obtain an uniaxial average stress state while face Z_1 (see figure 2b) is a traction-free surface. First, symmetry conditions are applied on hidden faces X_0, Y_0, Z_0. Then, homogeneous

Table 3: Material parameters for 316LN Steel, "MC-CP" model [28, 35].

Model	MC Crystal Plasticity						
Parameter	τ_0	K	n	Q	b	c	d
Value	60	10	10	15	1	10 000	400
Unit	MPa	$\mathrm{MPa\,s^{-n}}$		MPa		MPa	

Model	MC Interaction matrix					
Parameter	h_1	h_2	h_3	h_4	h_5	h_6
Value	1	1	0.6	12.3	1.6	1.8

Table 4: Material parameters for 316LN Steel, "ECP-CP" model [37].

Law	ECP Crystal Plasticity						
Parameter	τ_0	ρ_0	$\dot{\gamma}_0$	n	K	b	g_c
Value	24.46	1 770 000	4.10×10^{-11}	73.5	42	2.54×10^{-7}	3.86×10^{-6}
Unit	MPa	$\mathrm{mm^{-2}}$	$\mathrm{s^{-1}}$			mm	mm

Law	ECP Interaction matrix			
Parameter	a_0	a_1	a_2	a_3
Value	0.02	0.08	0.18	0.3

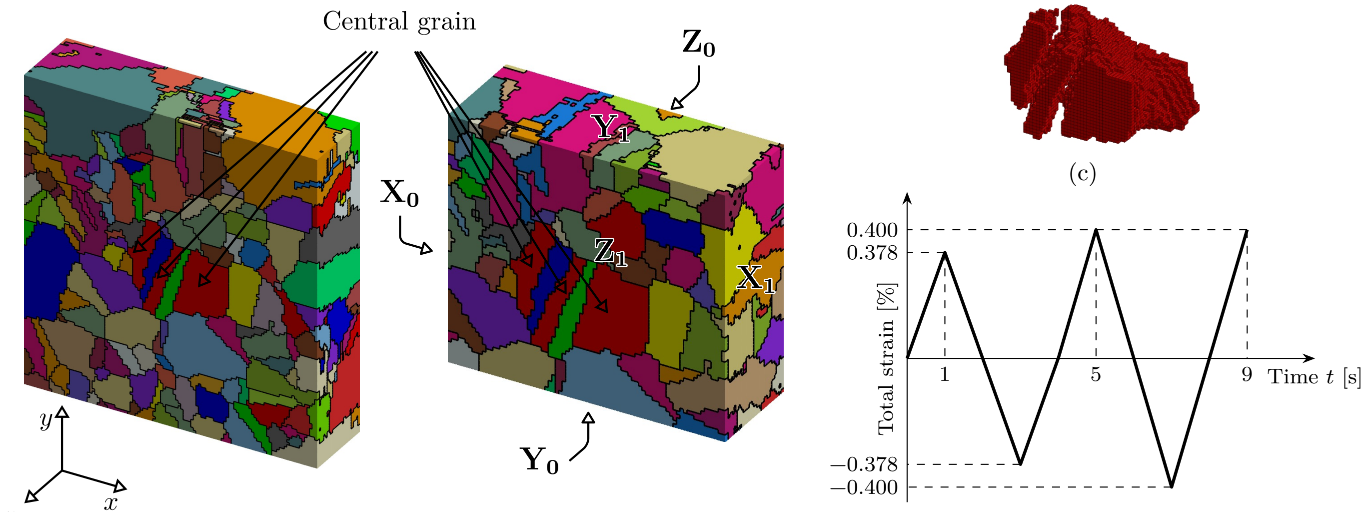

(a) (b) (d)

Figure 2: Meshes and boundary conditions of the "real" reconstructed aggregate: (a) large mesh (b) small mesh (c) central grain mesh (d) loading conditions.

normal displacement, i.e. in the loading direction x, is prescribed on face X_1 in order to simulate two cycles with the macroscopic total strain profile described in figure 2d and with a strain ratio $R_\varepsilon = -1$. For the first cycle, a total strain amplitude $\Delta\varepsilon/2 = 0.378\,\%$ has been applied; for the second cycle, a total strain amplitude is $0.4\,\%$ (in order to take into account non-constant total strain amplitude actually experienced during test performed with constant plastic strain amplitude, see section 2). Constraints on face Y_1 are defined in order to prescribe an homogeneous normal displacement so that this face remains flat.

4. Investigated parameters and variables

The second objective of this study is to analyse the influence of microstructural parameters on the fatigue cracks initiation, especially on the localisation of plastic deformation. A series of variables at different scales (values at the integration points and averaged values for grain) will be post-processed from the FE results.

- σ_{mises}, the equivalent von Mises stress, computed from the second invariant of deviatoric stress $\underset{\sim}{\boldsymbol{s}}$:

$$\sigma_{mises} = \sqrt{\frac{3}{2}\underset{\sim}{\boldsymbol{s}} : \underset{\sim}{\boldsymbol{s}}} \qquad \text{with } \underset{\sim}{\boldsymbol{s}} = \operatorname{dev} \underset{\sim}{\boldsymbol{\sigma}} \tag{15}$$

- ε^p_{mises}, the von Mises equivalent plastic strain:

$$\varepsilon^p_{mises} = \sqrt{\frac{2}{3}\underset{\sim}{\boldsymbol{\varepsilon}}^p : \underset{\sim}{\boldsymbol{\varepsilon}}^p} \tag{16}$$

- $\sum \gamma_{cum}$, the sum of cumulated viscoplastic slips over all the slip systems:

$$\sum \gamma_{cum} = \sum_s v^s \tag{17}$$

- $\gamma^{(i)}_{cum}$ with $i = 1, 2..., 12$: the accumulated plastic slip sorted in decreasing order of macroscopic Schmid factor (achieved by a pre-processing of crystallographic orientation data). Thus, $\gamma^{(1)}_{cum}$ corresponds to the accumulated plastic slip on the system which possesses the largest Schmid factor (i.e. primary slip system), while $\gamma^{(2)}_{cum}$ corresponds to the accumulated plastic slip on the slip system which possesses the second largest Schmid factor (i.e. secondary slip system), etc. It should be noted that $\gamma^{(1)}_{cum}$ will not always be greater than $\gamma^{(2)}_{cum}$ since the actual local stresses may promote plastic slip on the secondary system. It should be noted that in the whole paper, the primary slip system will always refer to the one with the highest macroscopic Schmid factor.

- N_γ, the number of active slip systems, defined by

$$\dot{v}^s > \dot{\gamma}_c = 0.75\,\frac{M_T \cdot \dot{\varepsilon}_{macro}}{5} \tag{18}$$

  where $\dot{\gamma}_c$ is a criterion parameter corresponding to $75\,\%$ of the average plastic strain rate at the local scale, i.e. at integration points. It depends on the Taylor factor M_T (about 3.1 for FCC polycrystals), the macroscopic loading axial strain rate $\dot{\varepsilon}_{macro}$, the number of independent internal variables needed to accommodate plastic strain (5 in our case).

- $|\tau^1/\sigma_{macro}|$: the ratio between the resolved shear stress on the primary slip system (1) and the macroscopic tensile stress.

- $|\tau^1/\tau^2|$: the ratio between the resolved shear stress on the primary slip system (1) and the one on secondary slip system (2).

- $\gamma^1_{cum}/\gamma^2_{cum}$: the ratio between the cumulative slip on the primary system γ^1_{cum} and the cumulative slip on the secondary system γ^2_{cum}.

- $\gamma^{max}_{cum}/\sum\gamma_{cum}$: the ratio between the maximum cumulative slip γ^{max}_{cum} and the sum of cumulated slip $\sum\gamma_{cum}$.

- $\underline{\gamma}_{surf}$ and $\tilde{\gamma}_{surf}$, the slip trace indicators, that takes into account local amount of plastic slip, the orientation of the glide with respect to both free surface normal and grain morphology. The projection of the plastic contribution of each slip system s on the free surface normal $\underline{\boldsymbol{n}}_{surf}$, noted γ^s_{surf}, provides an estimation of the height of the steps (intrusion–extrusion phenomenon) that can be created at the surface. Each one of these contributions is weighted by the parameter w_s, related to grain morphology. For each slip system s, the contribution is computed as:

$$\gamma^s_{surf} = \gamma^s \cdot w_s \cdot \underline{\boldsymbol{l}}^s \cdot \underline{\boldsymbol{n}}_{surf} \tag{19}$$

In the classic version, called PSM indicator and noted $\underline{\gamma}_{surf}$, no weight is applied with $w_s = 1$ whereas in the weighted version, called WPSM indicator and noted $\tilde{\gamma}_{surf}$, w_s corresponds to the distance from the free surface to the closest grain boundary along the slip direction of the system s (figure 3). This weight parameter represents the ability to issue dislocations to the surface and therefore to generate extrusions / intrusions. Then, the maximum contribution for all the systems, noted γ_{surf}, is stored with the associated slip system index s_{max} and the associated direction of the slip trace on the surface, $\underline{\boldsymbol{l}}_{surf}$.

$$s_{max} = \arg\max_s |\gamma^s_{surf}| \tag{20}$$

$$\gamma_{surf} = \gamma^{s_{max}}_{surf} \tag{21}$$

$$\underline{\boldsymbol{l}}_{surf} = \frac{\underline{\boldsymbol{n}}_{surf} \times \underline{\boldsymbol{n}}^{s_{max}}}{\left\|\underline{\boldsymbol{n}}_{surf} \times \underline{\boldsymbol{n}}^{s_{max}}\right\|} \tag{22}$$

$$\underline{\boldsymbol{\gamma}}_{surf} = \gamma_{surf} \cdot \underline{\boldsymbol{l}}_{surf} \tag{23}$$

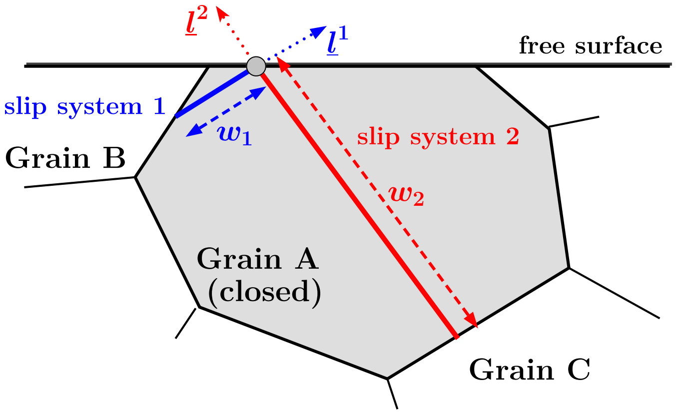

Figure 3: Schematic representation of the weight function, i.e. the distance from the surface to the grain boundary along slip direction, for two different slip systems.

It should be noted that the ratio $|\tau^1/\sigma_{macro}|$ corresponds to the local definition of the effective Schmid factor proposed by Sauzay [27], which reflects the stress heterogeneity within the polycrystal due to elastic and plastic anisotropy. The ratio $|\tau^1/\tau^2|$ allows to evaluate the effect of the actual local stresses on the order of activation of slip systems. The parameters N_γ, $\gamma^1_{cum}/\gamma^2_{cum}$ and $\gamma^{max}_{cum}/\sum\gamma_{cum}$ are intended to characterise the occurrence of multiple slip.

5. Results and discussion

Several simulations were carried out on the "real" aggregates, where the central grain corresponds to the cracked grain. First, the study focuses on the influence of the crystal plasticity model and of the simulated domain size on the local mechanical fields distribution. In fact, the results are very close for the quasi-physical model and the phenomenological model. Regarding domain size, the results seem to be affected only near grain boundaries. Specifically, for the central grain, the local fields are very similar regardless of the mesh.

Secondly, the parameters and variables described in section 4 are computed, in order to determine the most suitable to highlight the location of crack initiation. For this part of the study, the simulations are exclusively performed with the phenomenological model.

5.1. Influence of constitutive equations and aggregate size

The constitutive equations and the size of polycrystalline aggregates remain a key problem in micromechanical Finite Element Analysis (FEA). The influence of the constitutive law and of the simulated domain size was analysed through the study of local and global variables. In the following, the results are very close:

- in the aggregate, for both constitutive models;
- in the central grain, for the two domain sizes.

Figure 4 presents the hysteresis loops during the two simulated loading cycles, for both aggregate sizes and both constitutive models. As expected, the two meshes lead to similar results, demonstrating that the smaller mesh is enough to represent the macroscopic behaviour. Since the models have been calibrated independently on two different material batches, they provide a different response in terms of stress range. Specifically, the elastic domain exhibited by the ECP-CP model is a little too large, due to the absence of kinematic hardening in the model. It will later be demonstrated that this effect does not affect the validity of the comparison of the two models.

Table 5 provides the values of every stress and strain components at two different scales. They have been averaged on the whole aggregate (upper part of the table) and on the central grain (lower part) at the end of the second tensile loading ($t = 5$ s). These data confirm the curves of figure 4. An additional information is the fact that the loading is onedimensionnal in average for the aggregate, with the nullity of yy and zz components, and a negligible shear stress level. This is no longer exactly the case for the central grain, which exhibits a compressive in-plane stress σ_{yy}, and a tensile stress σ_{zz} normal to the surface, which value is more than 20 % of the tensile component. It shows that the grain "depth" is large, and that the stress component growths rapidly from zero on the surface to non negligible values in the bulk of the grain. One can note that the macroscopic strain components ε_{yy} and ε_{zz} do not fully correspond the expected Poisson's effect. Despite the fact there is no noticeable preferred crystallographic orientation in the 316LN steel, the low thickness of the aggregate in the z direction and the limited number of grains produce a local crystalline texture. Consequently, the aggregate cannot be considered as a representative volume element.

The influence of the constitutive law and of the size of the mesh were also investigated on a local scale. For this purpose, von Mises stresses σ_{mises} and the activity of the cumulated plastic slip for the primary system γ^1_{cum} were observed after the first cycle ($t = 5$ s) for both crystal plasticity laws and both domain sizes, respectively in figures 5 and 6. For each case, the contour plots are presented on the global mesh and on the central grain, that is extracted from the aggregate in order to have an enlarged view on the various levels. The results are in good qualitative agreement in the four situations. As observed at the macroscopic scale with table 5, the effect of the computed domain size remains low except at the domain boundaries. The maps in figure 5 show that von Mises stress values are qualitatively the same for the two constitutive equations, raising to wider extreme values with ECP-CP model (figures 5c and 5d), which provides more intense localisation. Figure 6 leads to a similar conclusion except that plastic slip values are globally higher ECP-CP model. This difference comes from the model: the "MC-CP" model represents plastic flow more precisely than the ECP-CP model for low strain

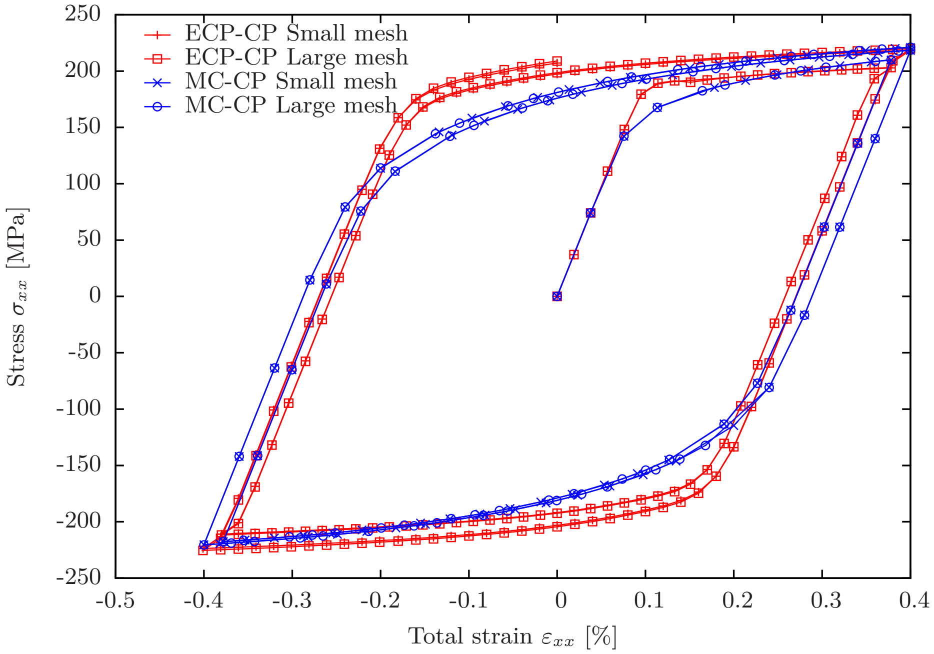

Figure 4: Cyclic responses of the aggregate for the small and large meshes with the “ECP-CP” and “MC-CP” behaviour laws.

Table 5: Mechanical states at the aggregate and central grain scale after the peak of tensile load of the first cycle ($t = 5\,\mathrm{s}$). “MC-CP” model, “ECP-CP” model.

Mean stress [MPa]	σ_{xx}	σ_{yy}	σ_{zz}	σ_{xy}	σ_{xz}	σ_{yz}
Aggregate - Small mesh “MC-CP”	217.0	0.0	0.0	−5.0	−1.0	0.0
Aggregate - Small mesh “ECP-CP”	218.5	0.0	0.0	−4.0	−2.0	0.0
Aggregate - Large mesh “MC-CP”	217.0	0.0	0.0	−6.0	0.5	−0.5
Aggregate - Large mesh “ECP-CP”	219.5	0.0	0.0	−6.0	0.5	−0.5
Central grain - Small mesh “MC-CP”	214.0	−16.5	43.5	−20.5	−4.5	14.5
Central grain - Small mesh “ECP-CP”	214.5	−17.5	49.0	−17.0	−11.5	17.0
Central grain - Large mesh “MC-CP”	217.5	−21.5	46.5	−30.0	−6.0	14.0
Central grain - Large mesh “ECP-CP”	220.5	−21.5	54.5	−30.0	−13.0	16.0

Mean strain [%]	ε_{xx}	ε_{yy}	ε_{zz}	ε_{xy}	ε_{xz}	ε_{yz}
Aggregate - Small mesh “MC-CP”	0.400	−0.143	−0.209	0.005	0.020	0.001
Aggregate - Small mesh “ECP-CP”	0.400	−0.135	−0.216	0.011	0.054	0.005
Aggregate - Large mesh “MC-CP”	0.400	−0.157	−0.194	−0.002	−0.001	−0.005
Aggregate - Large mesh “ECP-CP”	0.400	−0.153	−0.198	−0.003	0.000	−0.009
Central grain - Small mesh “MC-CP”	0.409	−0.114	−0.241	0.058	0.043	−0.030
Central grain - Small mesh “ECP-CP”	0.414	−0.109	−0.250	0.115	0.132	−0.047
Central grain - Large mesh “MC-CP”	0.412	−0.118	−0.240	0.045	0.038	−0.031
Central grain - Large mesh “ECP-CP”	0.416	−0.110	−0.249	0.085	0.127	−0.051

levels. Considering the mechanical fields within the central grain, it will be assumed that the influence of the aggregate size on the local results (see figures 5a, 5b, 5c and 5d) is small enough to justify the use of the smaller mesh.

5.2. Analysis of local fields in relation with experimental observations

Following the conclusions of the previous section, the subsequent analyses are exclusively performed on the small mesh and using the "MC-CP" crystal plasticity model. This section is dedicated to the analysis of local fields at the surface of the polycrystalline aggregate. The purpose is to discuss the parameters that play a role during the process of fatigue crack initiation and micropropagation. The various quantities defined in section 4 are used, and the results are discussed in relation with experimental observations.

The previous experimental study shows that for 66 % of the grains, transgranular cracks have been initiated along PSBs [10]. Thus, the first analysed parameters correspond to von Mises equivalent plastic strain ε^{p}_{mises} and the sum of cumulated viscoplastic slips $\sum \gamma_{cum}$ which associated contour maps are illustrated in figure 7 From a global point of view, a trend to develop localisation bands oriented at ±45° with respect to the loading direction is generally observed (see figure 7b). However, there is no specific deformation structure (such as PSBs) across the central grain. The largest amount of plastic flow is located at grain boundaries. As far as central grain is concerned, these parameters do not reach their maxima in the crack initiation zone, as observed in figure 7. These two parameters cannot be seen as being relevant to predict transgranular crack initiation.

Experimental observations also show that in 74 % of grains with transgranular cracks, the activated slip system has the highest Schmid factor. Thus, the primary and secondary accumulated slip activities at the free surface Z_1 and in the central grain at the end of the first cycle, ($t = 5\,\mathrm{s}$) are presented in figure 8. In the central grain, the activity γ^{1}_{cum} reaches the maximal value in the region where the crack appears, as shown by figure 8a. However, the maximum cumulated slip of the primary slip system is not obtained in the critical grain, but in its neighbor. Although large values can be found in the grains located at the border of the mesh, they are not considered as significant due to the perturbation in this zone. The activity of accumulated plastic slip for the secondary system γ^{2}_{cum} is reported in figure 8b. At the surface of the central grain, the activity of this system is moderate in the middle, but significant at the grain boundary, specifically near the left crystal twin. The numerical simulation indicates that the primary accumulated slip activity plays a predominant role in the prediction of crack initiation. This observation is in agreement with past experimental studies (see for instance [26, 38]) in which SEM observations were carried out on a large number of transgranular cracks initiated along PSBs, combined with EBSD measurements.

Moreover, it is interesting to study the evolution of the parameter γ^{1}_{cum} in the bulk, in order to determine its possible role during the micropropagation stage. Figure 9 illustrates this evolution within the central grain. The strong localised activity in the area of crack initiation subsides for a depth of 20 µm. According to experimental observations after 5000 cycles, the crack stops for a depth between 27 µm and 31 µm. The crack length after 5000 cycles is then equal to the depth of the significant plastic activity predicted by the numerical simulations on the non cracked aggregate after one cycle. However, it remains difficult to link these data since (i) the plastic zone can probably change between 2 and 5000 cycles, and (ii) the presence of microcracks causes a redistribution of local stresses and strains. In addition, there is no precise information about the chronology of crack propagation. Hence the crack might be still propagating at the end of the test. To conclude, the variable γ^{1}_{cum} seems to be a good candidate for the prediction of the crack initiation and propagation process.

Other parameters such as the presence of slip bands can be a factor which facilitates the crack initiation process. Figure 10 presents the number of active slip systems N_γ found in the simulation, as defined in section 4, at the free surface Z_1 and inside the central grain after the first cycle. Few grains exhibit noticeable variations of N_γ within them. In most grains, two active slip planes are observed on average and there are often more active slip systems at the grain boundaries. At the surface of the central grain, around the crack, the simulation reveals at least two active systems.

As a complementary analysis, the local stress deviation provided by the polycrystal is investigated through the primary and secondary resolved shear stresses (τ^1 and τ^2), which are presented as global and local map (figures 11a and 11b). Inside the cracked grain, the maximum resolved shear stress of the primary and secondary slip system are not observed in the crack initiation zone at the free surface but at the grain boundaries. The ratio between these two variables, noted $|\tau^1/\tau^2|$, gives a first information on the stress deviation induced by the polycrystal and neighborhood effect (figure 11c). However, analysing this variable is not obvious. Indeed, the stress deviation at the local scale may widen the gap between the activity of the primary and secondary systems. Consequently the ratio gets higher, even if the activity of the primary and of the secondary system differs within the grain (see figures 11a and 11b). Away from the area affected by the boundary conditions, the maximum values of the ratio are mainly reached near the grain boundaries and close to the central grain. Moreover, additional information is given by the ratio $|\tau^1/\sigma_{macro}|$. This value corresponds to the ratio between the resolved shear stress on the primary slip system τ^1 and the macroscopic tensile stress σ_{macro}, illustrated by figure 11d. Generally, the extreme values of this ratio are obtained at grain boundaries, where stress redistribution is enhanced. The mean value is about 0.32 which is consistent with the Taylor factor for FCC materials. It is noticeable that it corresponds to the predominant contour value. Especially in the central grain, where there is no

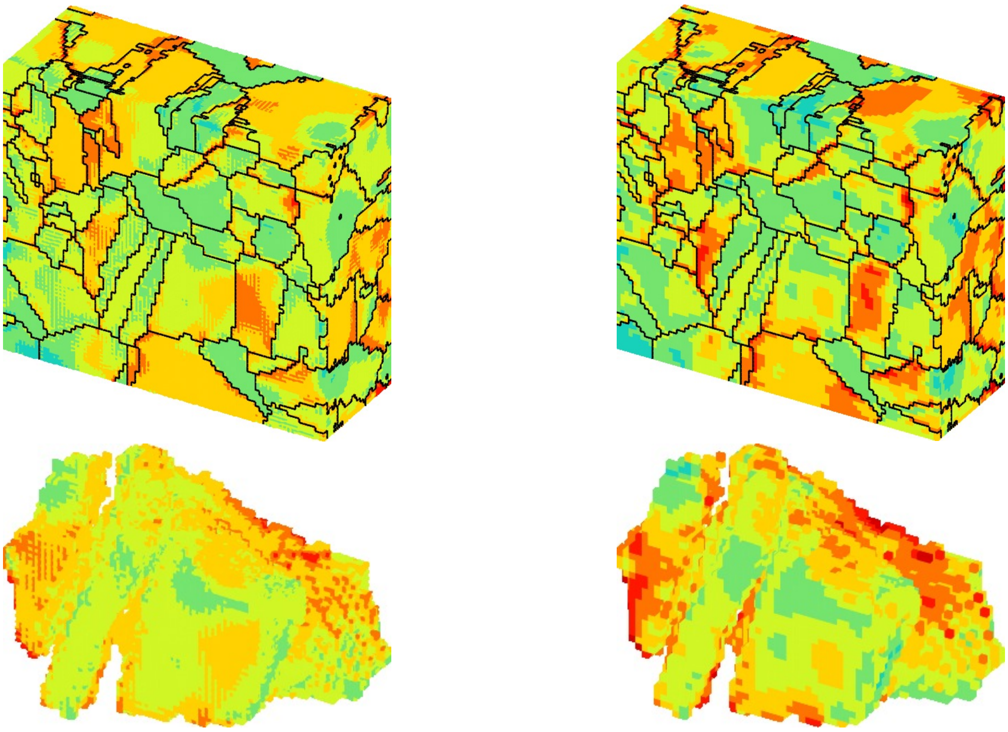

(a) Small mesh, “MC-CP”

(c) Small mesh, “ECP-CP”

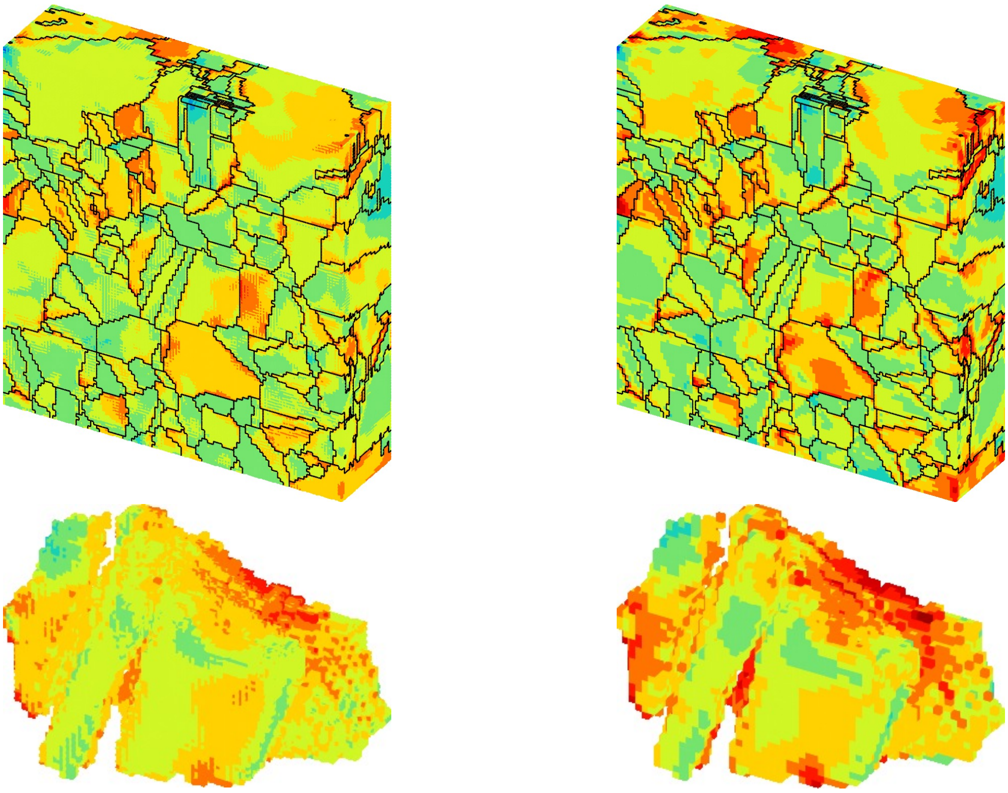

(b) Large mesh, “MC-CP”

(d) Large mesh, “ECP-CP”

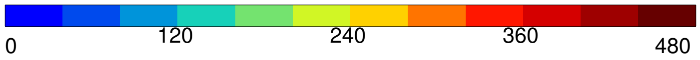

Figure 5: von Mises equivalent stress σ_{mises} at the free surface Z_1 and in the central grain after the first cycle ($t = 5\,\text{s}$).

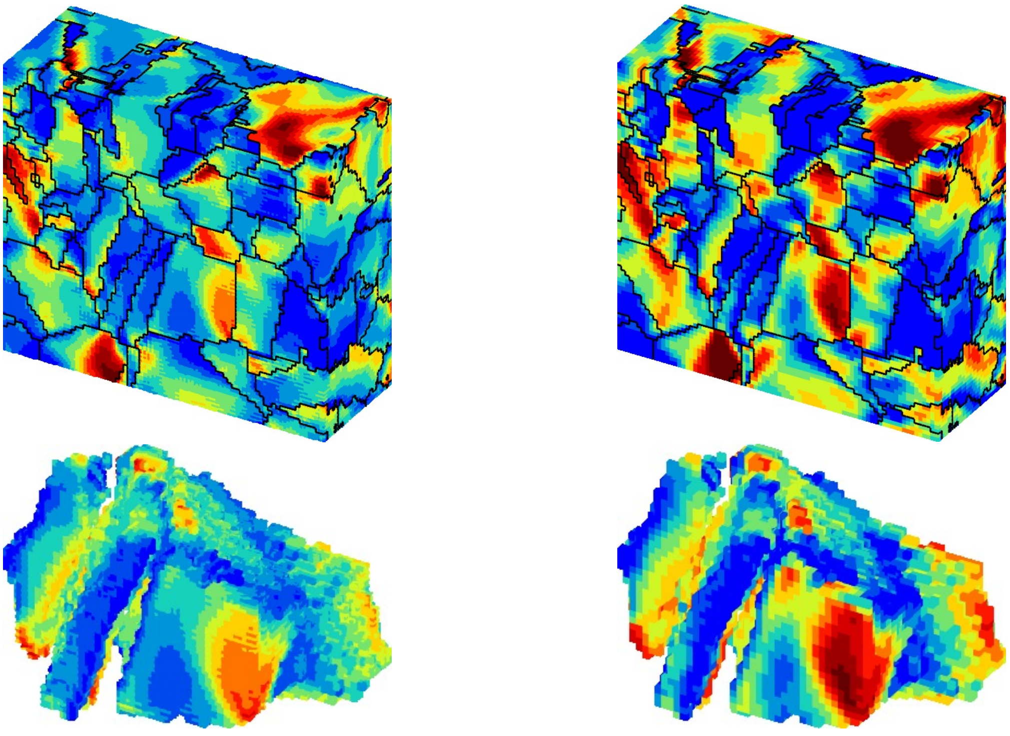

(a) Small mesh, “MC-CP” (c) Small mesh, “ECP-CP”

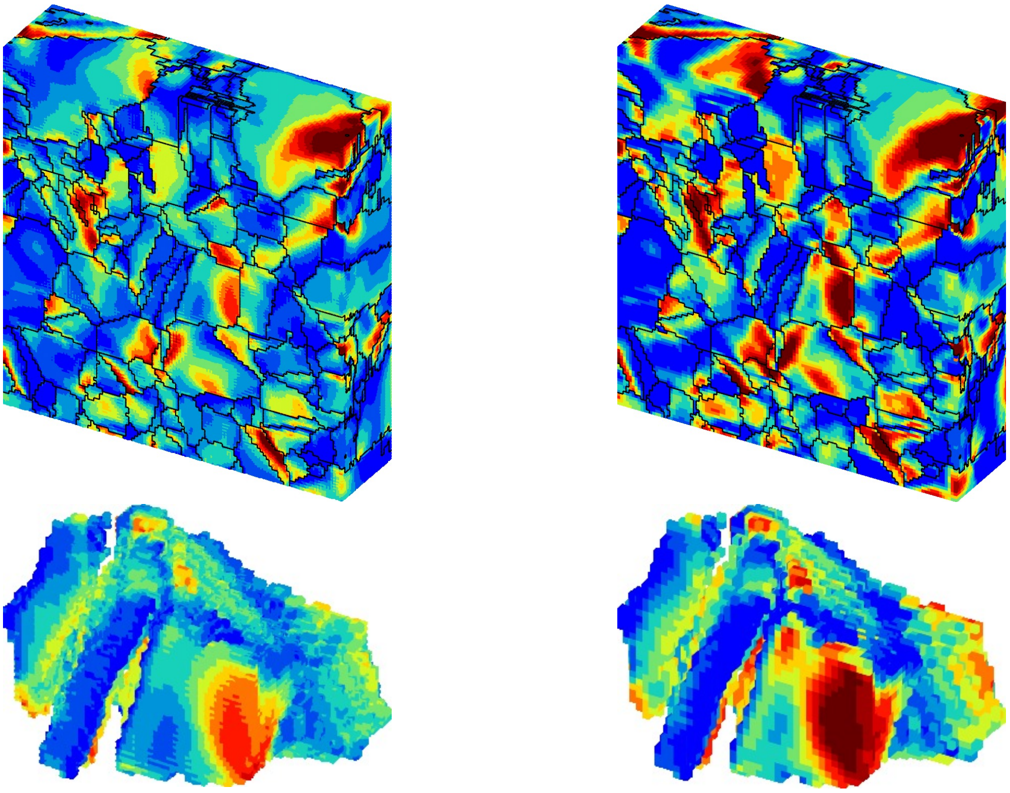

(b) Large mesh, “MC-CP” (d) Large mesh, “ECP-CP”

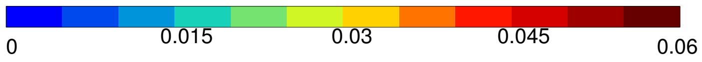

Figure 6: Activity of the cumulated plastic slip for the primary system γ^1_{cum} at the free surface Z_1 and in the central grain after the first cycle ($t = 5\,\mathrm{s}$).

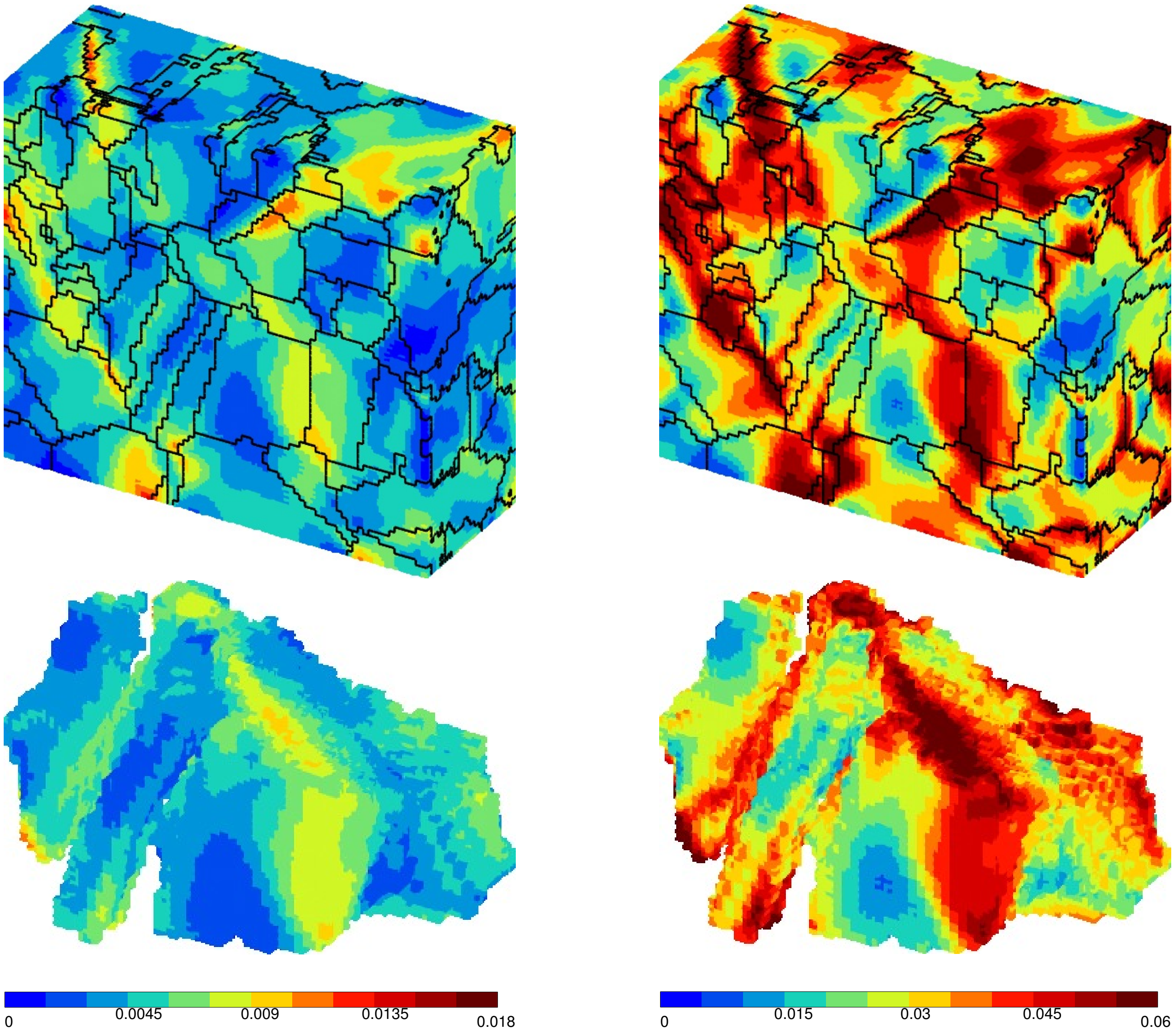

(a) ε^{p}_{mises} (b) $\sum \gamma_{cum}$

Figure 7: (a) von Mises equivalent plastic strain ε^{p}_{mises} (b) Sum of cumulated viscoplastic slips $\sum \gamma_{cum}$ at the free surface Z_1 and in the central grain after the first cycle ($t = 5\,\mathrm{s}$) for the small mesh with the “MC-CP” model.

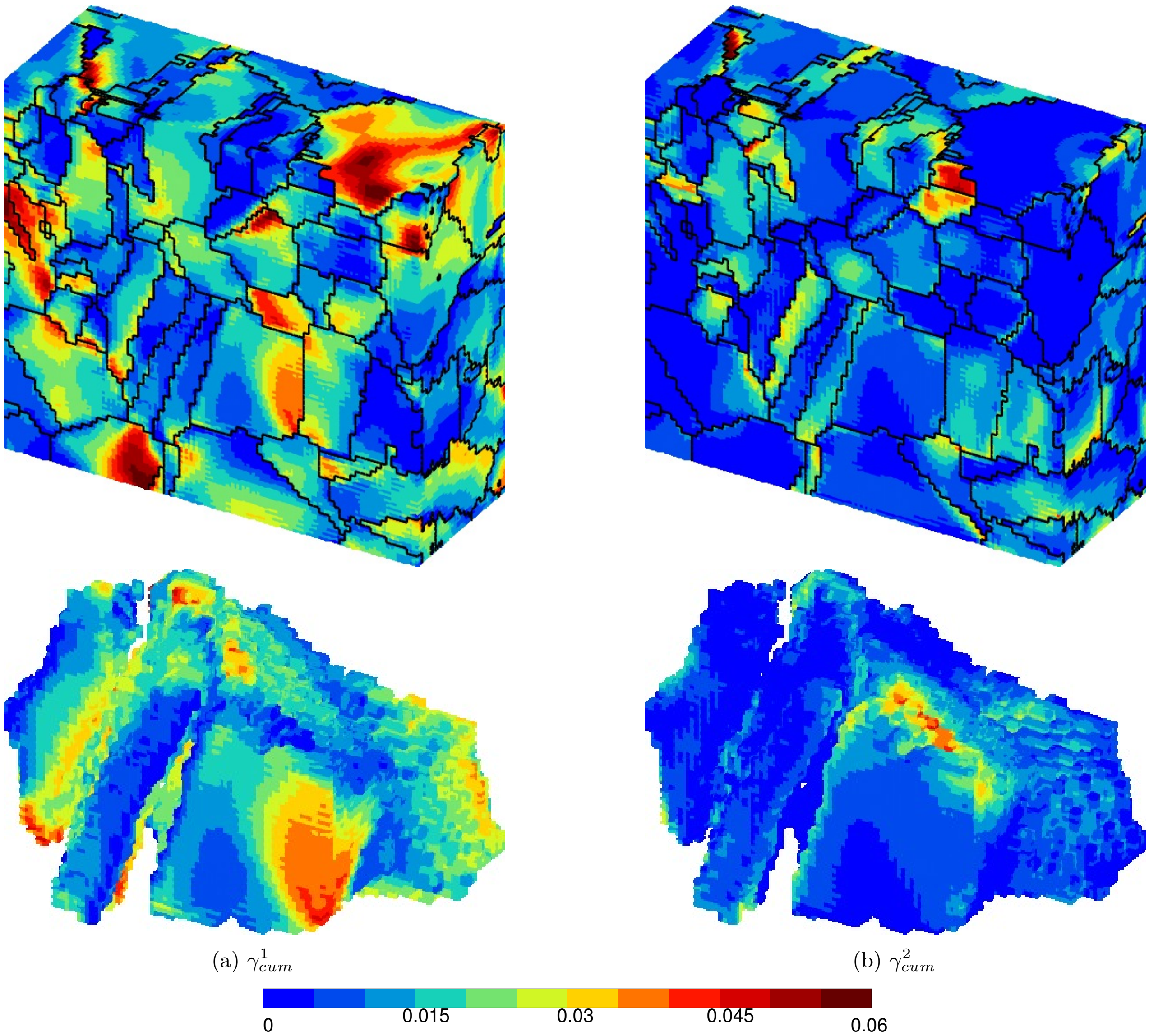

(a) γ^1_{cum} (b) γ^2_{cum}

Figure 8: Activity of the cumulated plastic slip (a) Primary system γ^1_{cum} (b) Secondary system γ^2_{cum} at the free surface Z_1 and in the central grain after one cycle ($t = 5\,\mathrm{s}$) for the small mesh with the "MC-CP" model.

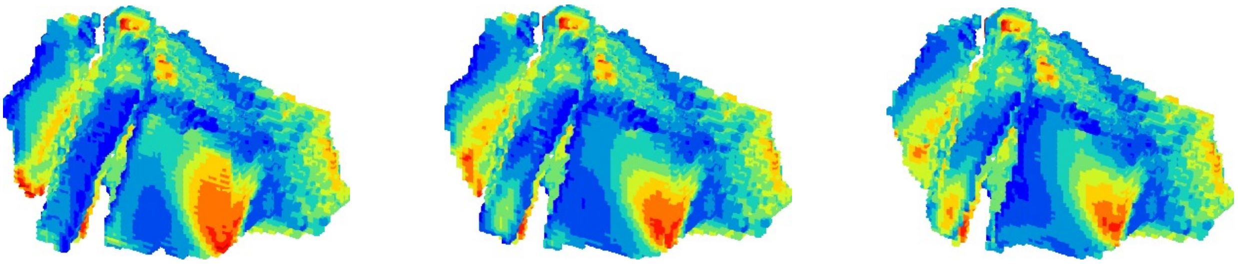

(a) 0 µm

(b) 5 µm

(c) 10 µm

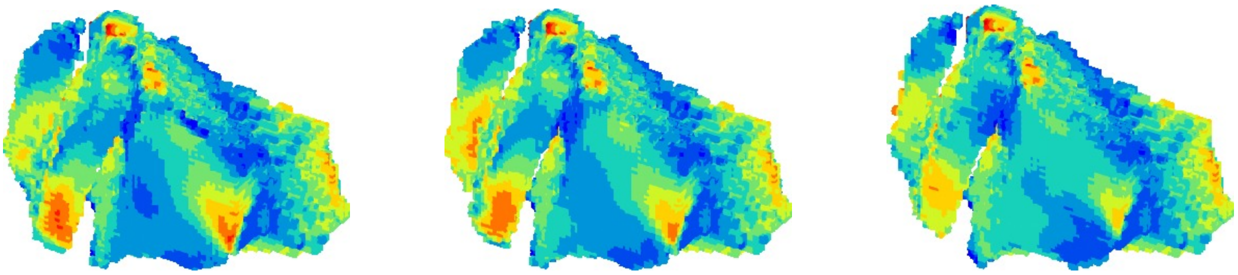

(d) 15 µm

(e) 20 µm

(f) 25 µm

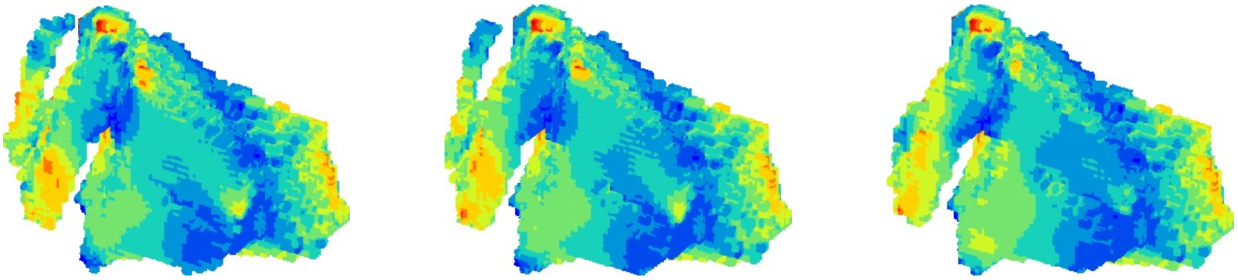

(g) 30 µm

(h) 35 µm

(i) 40 µm

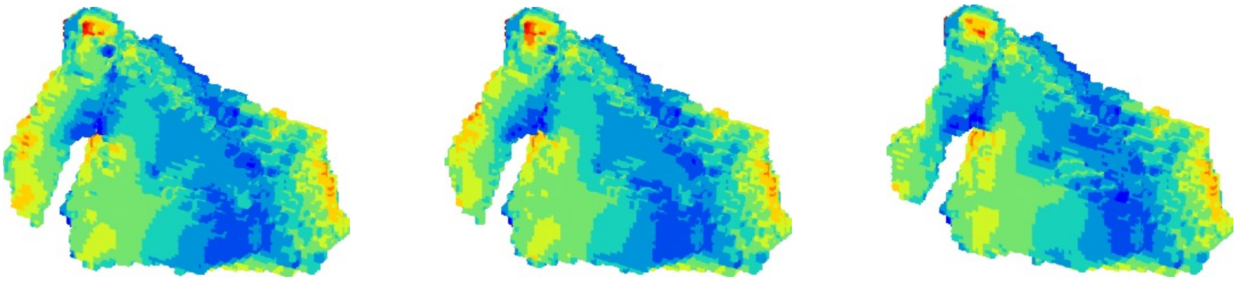

(j) 45 µm

(k) 50 µm

(l) 55 µm

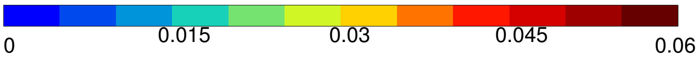

Figure 9: Activity of the cumulated plastic slip on the primary system γ^1_{cum} at different depth within the central grain after the first cycle ($t = 5\,\mathrm{s}$) for the small mesh with the “MC-CP” model.

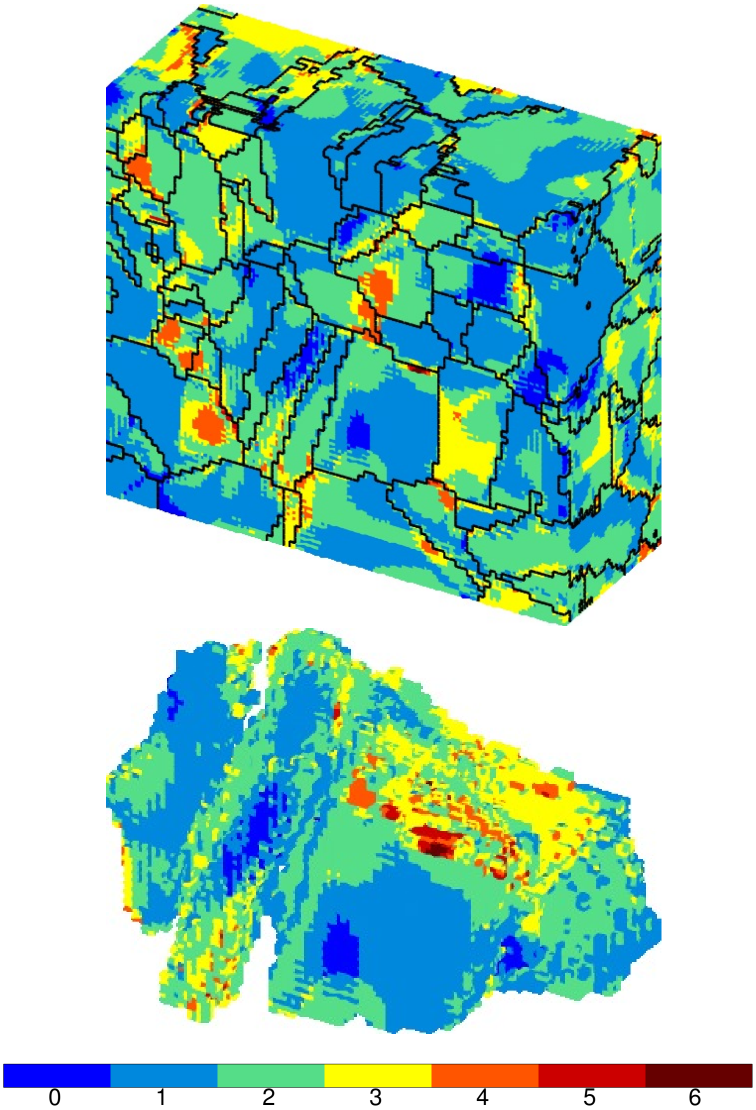

Figure 10: Number of active slip systems N_γ in the Z_1 free surface and at the central grain after the first cycle for the small mesh with the "MC-CP" model.

significant effect of stress deviation on the primary resolved shear stress at the surface in the area of crack initiation.

Finally, the single or multiple slip appearance is investigated within the central grain. Two parameters are used and presented in figure 12: the ratio between the cumulative slip on the primary system γ^1_{cum} and secondary system γ^2_{cum}, noted $\gamma^1_{cum}/\gamma^2_{cum}$, and the ratio $\gamma^{max}_{cum}/\sum\gamma_{cum}$ between the maximum cumulative slip γ^{max}_{cum} and the sum of cumulated slip $\sum\gamma_{cum}$. At the free surface Z_1 of the central grain, the contour map presented in figure 12a highlights the occurrence of single slip around the crack area. This result is confirmed by the contour map in figure 12b.Thus, single slip is observed at the free surface of the cracked grain, specifically in the area of the crack.

The last type of variable is likely to characterise the possibility for a grain to develop intrusions or extrusions. The contour map of this indicator (γ_{surf}) on the free surface Z_1 at the end of the first cycle is obtained by drawing color segments, the orientation of which is determined by the surface trace of the plane $\underline{\boldsymbol{l}}_{surf}$. The intensity is characterised by a color scale. Figure 13a shows the full aggregate, meanwhile figure 13b presents a zoom on the central grain. The red lines represent the location and orientation of the cracks observed experimentally. These maps are also used to locate critical areas. Most of the grains have only one computed single trace, but two different slip planes can be observed in some cases (six grains i.e. about 10 %). These numbers are in excellent agreement with the experimental results [10] for which in most of the grains, only one slip trace could be identified. Also two different slip systems were experimentally observed in 10 % of the grains whereas no slip traces were detected for 15 % of the grains.

The traces are generally perpendicular or orientated at 45° with respect to the loading direction. Central grain contains traces for a single plane with a high intensity relative to its neighbors. The orientation of the planes in cracked grain is in perfect agreement with experimental observations, as shown in figure 1 and 13. This result is also in agreement with several studies demonstrating that crack initiation occurs along PSBs in 316LN type austenitic stainless steel subjected to low cycle fatigue, and also at grain boundary and twin boundaries [38, 39]. However, this parameter does not allow to specifically shed the light to the cracked grain.

An improved slip trace indicator $\tilde{\gamma}_{surf}$, taking into account the contribution of each slip system according to the distance between surface and the next grain boundary along slip direction is now examined. Figure 13 presents a comparison of the initial intrusion-extrusion fatigue indicator and the new weighted version, after the first cycle ($t = 5\,\mathrm{s}$). The weighted version allows to isolate the grain number 88 which is exactly the one where the crack initiates in the experiment (as recalled in figure 1 and figure 13b). The WPSM indicator appears then definitely as the most relevant candidate to predict both the location of the initiation and the orientation of the transgranular microcracks , following the example of a directional type of Hall-Petch effect [40]. The introduction of the distance from the surface to the next grain boundary along the slip directions of the critical plane allows to highlight the proper critical grain. In absence of this weighting factor, the plastic slip intensity is not a discriminating parameter [10].

6. Conclusion

The mechanism of microstructurally short crack initiation and propagation remains a difficult issue where many variables come into play. The aim of this paper was to characterise the parameters responsible for the transgranular microcrack initiation and propagation. The study focused on the local mechanism at the free surface of a real polycrystalline aggregate, made of 316LN stainless steel, using Finite Element Crystal Plasticity (FECP). These simulation results were compared with the experimental observations to determine the key parameter driving the crack initiation process. Before analysing the local mechanisms, two material behaviour models and the choice of the size of the simulated domain of the aggregate were discussed. Both quasi-physical and phenomenological crystal plasticity models gave the same qualitative results and it was shown that the computed domain size should be chosen large enough to avoid the effects of boundary conditions.

Some parameters and variables were analysed and compared to the experimental observations and attempt to determine the parameters closely linked to transgranular microcracks initiation. Some classical global parameters (such as the equivalent von Mises stress, the equivalent von Mises plastic strain, the sum of cumulated viscoplastic slips, the deviation of local stresses in the polycrystal) do not appear to be the relevant parameters.

The analyses performed in this study lead to the conclusion that the initiation of transgranular microcracks seems to be governed by:

- the accumulated slip on the primary system;
- the presence of single slip;
- a slip direction consistent with the free surface normal;
- a long distance from the surface to the grain boundary in the slip direction.

The intrusion-extrusion weighted parameter allowed us to precisely select the critical grain. Additional studies must be now completed. First, the analysis should be extended to a larger number of aggregates with more grains. This would allow to make a statistical study and to confirm the way the geometry and the crystallography of the grain influence the process of crack initiation. Indeed, the grain size and the neighbouring grains have an influence on plastic activity [14, 41]. Next, since the neighborhood of the grain plays a significant role, the analysis should include the first neighbors. Finally, simplifications were made in

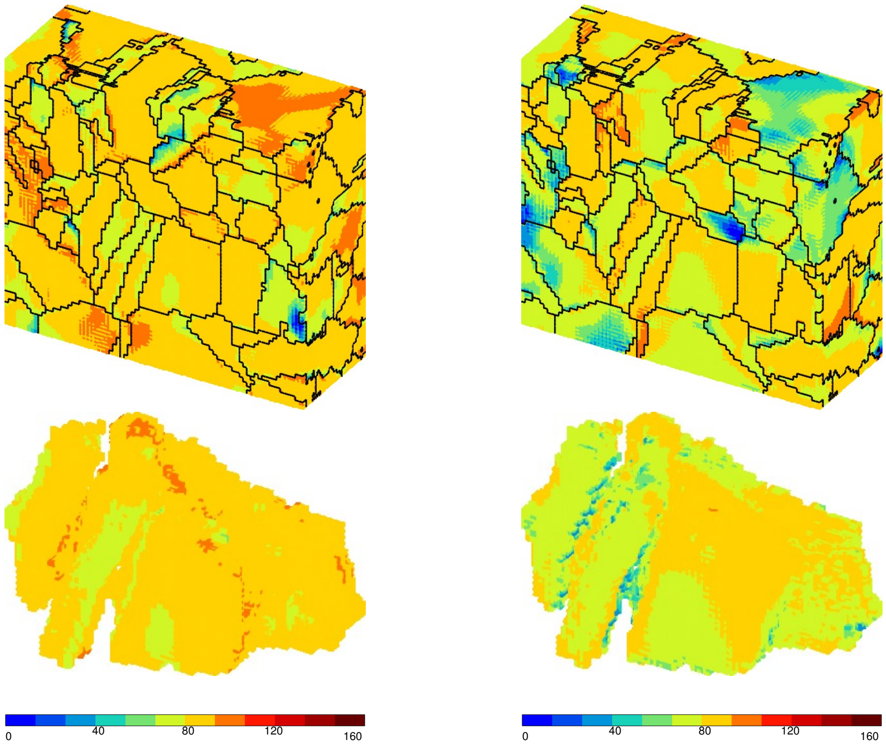

(a) $|\tau^1|$ (b) $|\tau^2|$

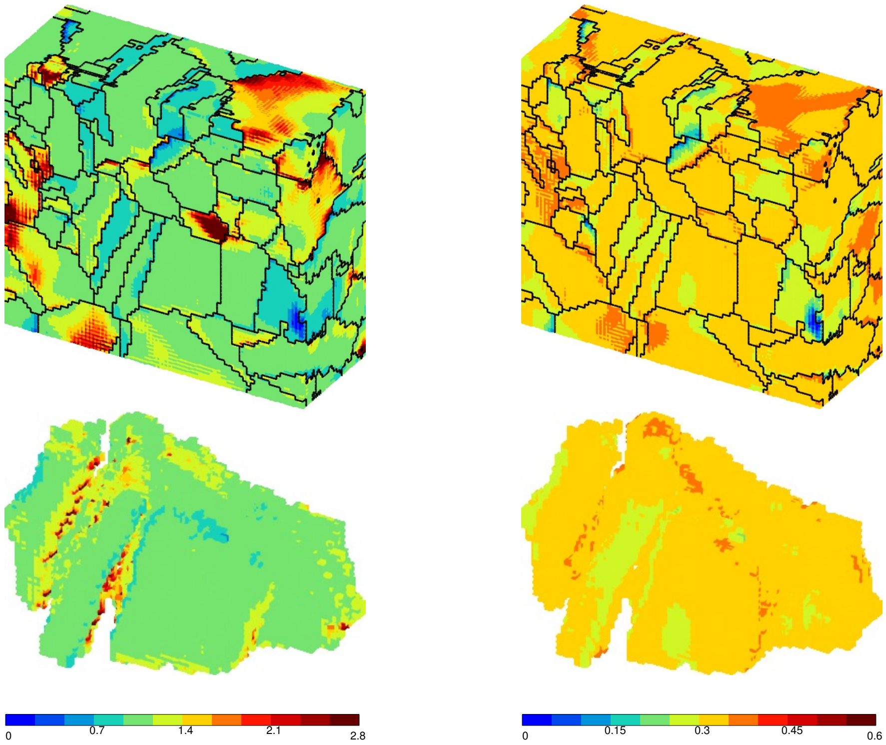

(c) $|\tau^1/\tau^2|$ (d) $|\tau^1/\sigma_{macro}|$

Figure 11: (a) Primary slip system (b) Secondary slip system. Ratio between (c) the resolved shear stress on the primary slip system (1) and the macroscopic tensile stress (d) the resolved shear stress on the primary slip system (1) and the one on secondary systems (2) on the free surface Z_1 and at the central grain after the first cycle ($t = 5\,\mathrm{s}$) for the small mesh with the "MC-CP" model.

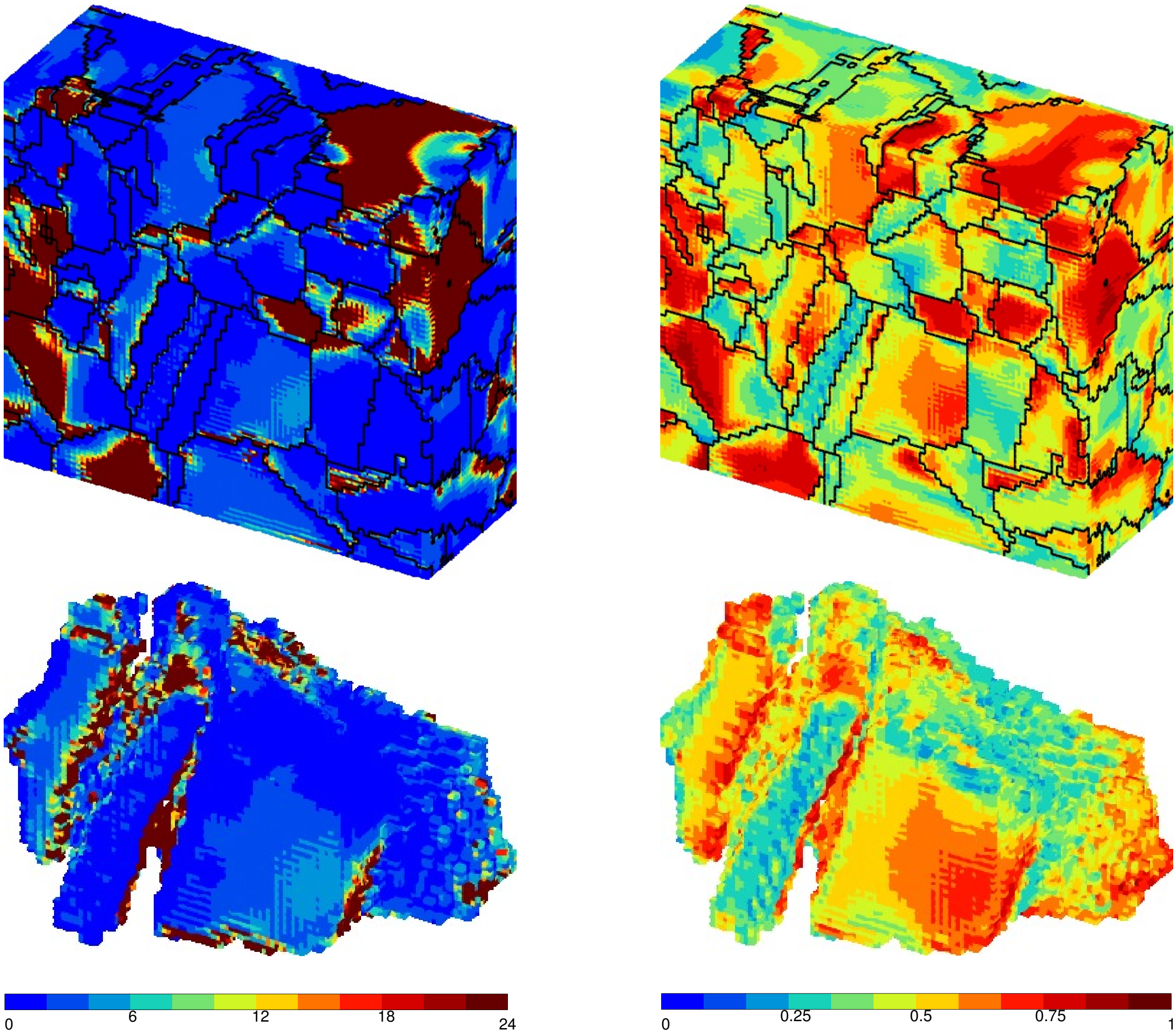

(a) $\gamma^1_{cum}/\gamma^2_{cum}$ (b) $\gamma^{max}_{cum}/\sum\gamma_{cum}$

Figure 12: (a) Ratio $\gamma^1_{cum}/\gamma^2_{cum}$ between the cumulative slip on the primary system and the cumulative slip on the secondary system. (b) Ratio $\gamma^{max}_{cum}/\sum\gamma_{cum}$ between the maximum cumulative slip and the sum of cumulative slip at the free surface Z_1 and in the central grain after the first cycle ($t = 5\,\mathrm{s}$) for the small mesh with the "MC-CP" model.

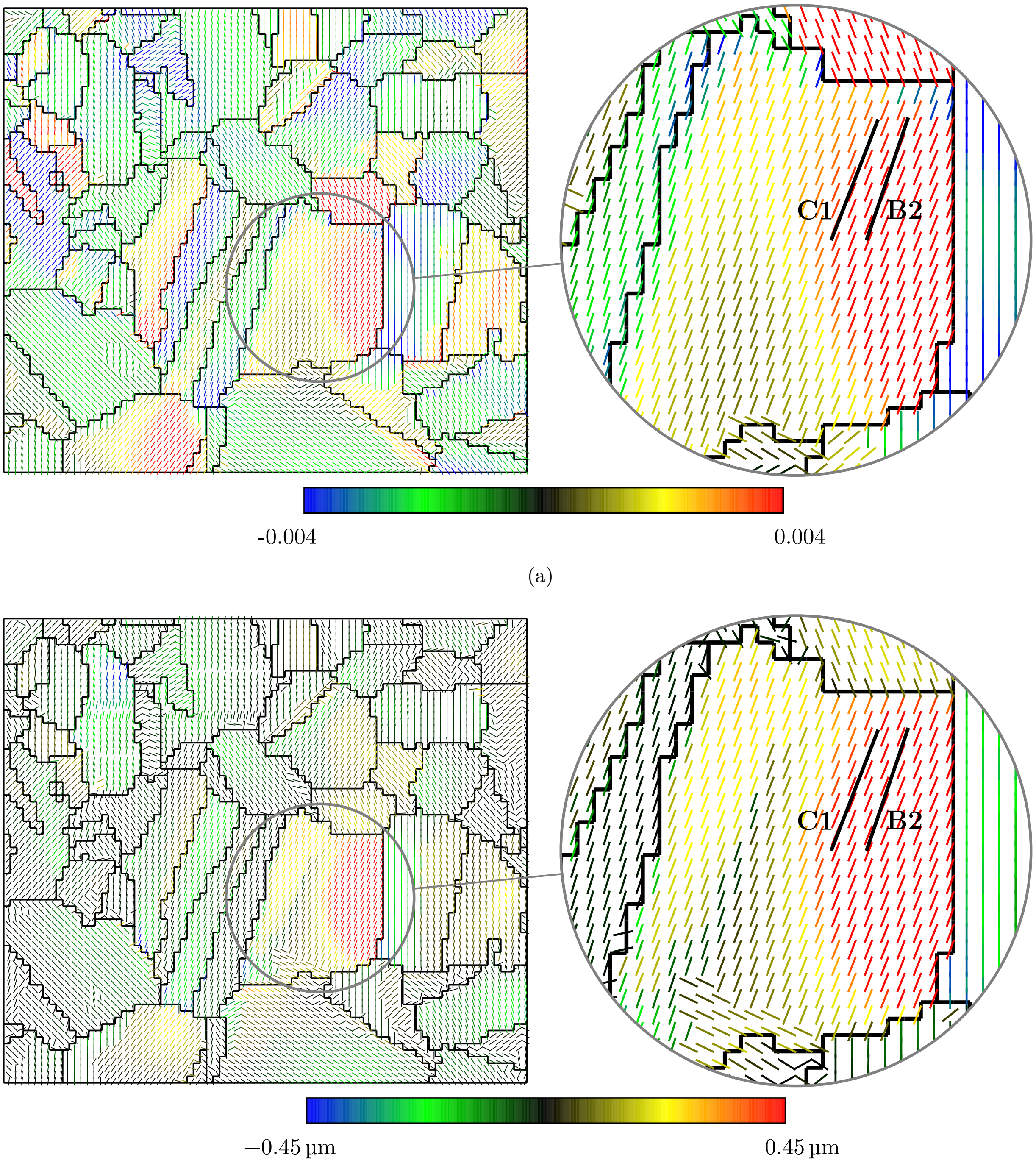

(a)

(b)

Figure 13: Intrusion-extrusion fatigue indicator (a) without and (b) with distance to grain boundary weighting, at the free surface Z_1 and in the central grain (zoom window) at the of the first cycle ($t = 5\,\mathrm{s}$). The black thick lines represent the position of the cracks observed experimentally for the small mesh with the “MC-CP” model.

this study, such as the assumption of a “perfect” (flat) free surface, which do not exactly reflect common surface states. Indeed, introducing a rough surface in the numerical model can change the localisation patterns of the local mechanical fields [42]. Since the microstructure is the source of transgranular and intergranular cracks, a similar study could be extended to intergranular cracks.

Acknowledgement

The work presented in this paper was supported by the French National Agency for Research (ANR), in the framework of the project AFGRAP ANR-08-MAPR-0024. Additionally, the authors would like to thank François Curtit and Jean-Michel Stéphan from EDF R&D for their involvement in the launching and monitoring of this project as well as their helpful comments and suggestions.

[1] K. Miller, The behaviour of short fatigue cracks and their initiation. Part II–A General summary, Fatigue and Fracture of Engng Mat and Struct 10 (1987) 93–113.

[2] P. Forsyth, C. Stubbington, The structure of slip band extrusion revealed by transmission electron microscopy, Acta Metall. 8 (1960) 811–814.

[3] U. Essmann, U. Gösele, H. Mughrabi, A model of extrusions and intrusions in fatigued metals: I. Point-defect production and the growth of extrusions, Phil. Mag. 44 (1981) 405–426.

[4] B.-T. Ma, C. Laird, Overview of fatigue behavior in copper single crystals: I. Surface morphology and stage I crack initiation sites for tests at constant strain amplitude, Acta Mat. 37 (1989) 325–336.

[5] C. Blochwitz, J. Brechbühl, W. Tirschler, Analysis of activated slip systems in fatigued nickel polycrystals using the EBSD–technique in the scanning electron microscope, Mater. Sci. Eng. A210 (1996) 42–47.

[6] J. Man, K. Obrtlik, P. J., Extrusions and intrusions in fatigued metals. part 1. state of the art and history, Philosophical Magazine 16 (2009) 1295–1336.

[7] K. Chan, J. Lankford, The role of microstructural dissimilitude in fatigue and fracture of small cracks, Acta Metall. 36 (1988) 193–206.

[8] M. Mineur, P. Villechaise, J. Mendez, Influence of the crystalline texture on the fatigue behavior of a 316l austenitic stainless steel, Mater. Sci. Eng. A 286 (2000) 257–268.

[9] P. Mu, V. Aubin, I. Alvarez-Armas, A. Armas, Influence of the crystalline orientations on microcrack initiation in low-cycle fatigue, Mater. Sci. Eng. A 573 (2013) 45–53.

[10] L. Signor, P. Villechaise, T. Ghidossi, E. Lacoste, M. Gueguen, S. Courtin, Influence of local crystallographic configuration on microcrack initiation in fatigued 316LN stainless steel: experiments and crystal plasticity finite elements simulations, Mater. Sci. Eng. A 649 (2016) 239–249.

[11] T. Lin, K. Wong, N. Teng, S. Lin, Micromechanic analysis of fatigue band crossing grain boundary, Mater. Sci. Eng. A246 (1998) 169–179.

[12] G. Potirniche, S. Daniewicz, Analysis of crack tip plasticity for microstructurally small cracks using crystal plasticity theory, Engng Fracture Mechanics 70 (2003) 1623–1643.

[13] V. Bennett, D. McDowell, Crack tip displacements of microstructurally small cracks in single phase ductile polycrystals, Engng Fracture Mechanics 70 (2003) 185–207.

[14] Y. Guilhem, S. Basseville, F. Curtit, J.-M. Stéphan, G. Cailletaud, Investigation of the effect of grain clusters on fatigue crack initiation in polycrystals, Int. J. Fatigue 32 (2010) 1748–1763.

[15] F. Barbe, L. Decker, D. Jeulin, G. Cailletaud, Intergranular and intragranular behavior of polycrystalline aggregates. Part I: FE model, Int. J. of Plasticity 17 (4) (2001) 513–536.

[16] C. Przybyla, D. McDowell, Microstructure-sensitive extreme value probabilities for high cycle fatigue of Ni-base superalloy IN100, Int. J. of Plasticity 26 (2010) 372–394.

[17] Y. Guilhem, S. Basseville, F. Curtit, J.-M. Stéphan, G. Cailletaud, Numerical investigations of the free surface effect in three-dimensional polycrystalline aggregates, Computational Materials Science 70 (2013) 150–162.

[18] F. Dunne, A. Wilkinson, R. Allen, Experimental and computational studies for low cycle fatigue crack nucleation in a polycrystal, Int. J. of Plasticity 23 (2007) 273–295.

[19] M. Zhang, F. Bridier, P. Villechaise, J. Mendez, D. McDowell, Simulation of slip band evolution in duplex Ti-6Al-4V, Acta Mat. 58 (2010) 1087–1096.

[20] L. Méric, G. Cailletaud, Single crystal modeling for structural calculations. Part 2: Finite element implementation, J. of Engng. Mat. Technol. 113 (1991) 171–182.

[21] D. Peirce, R. Asaro, A. Needleman, Material rate dependence and localized deformation in crystalline solids, Acta Metall. 31 (1983) 1951–1976.

[22] C. Teodosiu, J.-L. Raphanel, L. Tabourot, Finite element simulation of the large elastoplastic deformation of multicrystals, in: 5th MECAMAT Int. Seminar on Large Plastic Deformations: Fundamental Aspects and Applications to Metal Forming, MECAMAT, Fontainebleau, France, 1993, pp. 153–168.

[23] M. Groeber, S. Ghosh, M. Uchic, D. Dimiduk, A framework for automated analysis and simulation of 3D polycrystalline microstructures., Part I: statistical characterization. Acta Mater 56 (2008) 1257–1273.

[24] M. A. Groeber, Digital Representation of Materials Grain Structure, Springer US, Boston, MA, 2011, Ch. 3, pp. 53–97.

[25] M. Uchic, Serial Sectioning Methods for Generating 3D Characterization Data of Grain- and Precipitate-Scale Microstructures, Springer US, Boston, MA, 2011, Ch. 2, pp. 31–52.

[26] M. Mineur, Conditions locales d’amorçage des fissures de fatigue dans un acier inoxydable de type 316L : aspects cristallographiques (EBSD), Ph.D. thesis, École Nationale Supérieure de Mécanique et d’Aérotechnique (2000).

[27] M. Sauzay, Effet de l’anisotropie élastique cristalline sur la distribution des facteurs de Schmid à la surface des polycristaux, C.R. Mécanique 334 (2006) 353–361.

[28] H. Huntington, The elastic constants of crystals, Solid State Physics 7 (1958) 213–351.

[29] J. Besson, G. Cailletaud, J.-L. Chaboche, S. Forest, Nonlinear Mechanics of Materials, Springer, 2009.

[30] P. Franciosi, The concepts o,f latent hardening and strain hardening in metallic single crystals, Acta Metall. 33 (1985) 1601–1612.

[31] S. Queyreau, G. Monnet, B. Devincre, Slip systems interactions in α-iron determined by dislocation dynamics simulations, Int. J. of Plasticity 25 (2009) 316–377.

[32] G. Monnet, A crystalline plasticity law for austenitic stainless steels, Tech. Rep. H-B60-2008-04690-EN, EDF R&D (2009).

[33] C. Gérard, Mesures de champs et identification de modèles de plasticité cristalline, Ph.D. thesis, Université Paris XIII (2008).

[34] C. Gérard, B. Bacroix, M. Bornert, G. Cailletaud, J. Crépin, S. Leclercq, Hardening description for FCC materials under complex loading paths, Computational Materials Science 45 (2008) 751–755.

[35] Y. Guilhem, Etude numérique des champs mécaniques locaux dans les agrégats polycristallins d’acier 316l sous chargement de fatigue, Ph.D. thesis, Ecole des Mines de Paris, ParisTech (2011).

[36] Abaqus user’s manual, RI: Hibbitt, Karlsson & Sorensen, INC, version 6.11 (2011).

[37] J. Schwartz, O. Fandeur, C. Rey, Fatigue crack initiation modeling of 316LN steel based on non local plasticity theory, Procedia Engineering 2 (2010) 1353–1362.

[38] P. Mu, V. Aubin, I. Alvarez-Armas, A. Armas, Influence of the crystalline orientations on microcrack initiation in low-cycle fatigue, Mat. Sci. Eng. 573 (2013) 45–53.

[39] M. Mineur, P. Villechaise, J. Mendez, Influence of the crystalline texture on the fatigue behavior of a 316L austenitic stainless

steel, Mater. Sci. Eng. A286 (2000) 257–268.

[40] N. Petch, The cleavage strength of polycrystals, Journal of the Iron and Steel Institute 5 (1953) 25–28.

[41] J. Man, K. Obrtlík, C. Blochwitz, J. Polák, Atomic force microscopy of surface relief in individual grains of fatigued 316L austenitic stainless steel, Acta Mat. 50 (2002) 3767–3780.

[42] Y. Guilhem, S. Basseville, H. Proudhon, G. Cailletaud, Effects of surface roughness on plastic strain localization in polycrystalline aggregates, in: 2nd International Symposium on Fatigue Design & Material Defects (FDMD II), Paris, France, 2014, paper no 06009.